ADVANCED FUNCTIONAL MATERIALS
www.afm-journal.de

Metal–Organic Frameworks Photocatalyst Through Plasmon-Induced Hot-Electrons

Tolga Zorlu, I. Brian Becerril-Castro, Ana Sousa-Castillo, Begoña Puértolas, Lucas V. Besteiro, Zhiming Wang, Alexander Govorov, Miguel A. Correa-Duarte, and Ramon A. Alvarez-Puebla**

Plasmonic metal–organic frameworks (plasmonic-MOFs) ingeniously meld the homogeneous and vast porosity of MOFs with the distinctive plasmonic characteristics of metallic nanoparticles (NPs), creating a powerful synergy. This innovative combination is leveraged for enhanced plasmon-induced hot-electron photocatalysis, particularly within polystyrene beads adorned with silver nanoparticles (AgNPs) and encapsulated by zeolitic imidazolate framework-8 (ZIF-8). The strategic incorporation of AgNPs into this composite material generates hot carriers, significantly enhancing the catalytic performance of ZIF-8. This approach not only exemplifies the potential for advanced photocatalytic processes of MOFs, but also paves the way for groundbreaking applications in environmental remediation and sustainable chemistry.

1. Introduction

Metal–Organic Frameworks (MOFs) are porous materials characterized by their homogeneous pores, which are meticulously constructed through the coordination of organic linkers and metal ions.[1] MOFs have showcased their versatility across a wide spectrum of applications, including separation, drug delivery, or catalyst supports, either as standalone materials or in combination with other materials to form composites.[2] Specifically, plasmonic nanoparticles encapsulated with MOFs have been effectively utilized in drug delivery,[3] the capture and/or separation of pollutants,[4] or the ultrasensitive analysis of small molecules and ions using surface-enhanced Raman scattering spectroscopy (SERS).[5] This latter application is rooted in the generation of localized surface plasmon resonances (LSPRs) occurring within embedded metallic nanoparticles (NPs) when illuminated with light.[6] The excitation of LSPRs also facilitates the emission from the metal of a fraction of the oscillating electrons composing the plasmonic resonance, those with high excess energies and commonly referred to as "hot electrons," allowing their transfer to neighboring materials, such as semiconductors.[7] This unique process has spurred the creation of state-of-the-art plasmonic-semiconductor composites, meticulously designed to augment photocatalytic efficiency.[8] Although MOFs are celebrated for exhibiting semiconductor behavior,[9] their catalytic performance often falls short when compared to conventional photocatalytic materials like titanium oxide. This shortcoming has somewhat limited their appeal in specific photocatalytic contexts.[10] However, the strategic inclusion of metallic NPs within MOFs can dramatically enhance the photocatalytic capabilities of the MOFs themselves by facilitating the injection of hot carriers. This innovative approach capitalizes on the exceptional ability of MOFs to pump electrons, combined with their naturally high surface area and uniform porosity. Consequently, this leads to the synthesis of materials with markedly improved photocatalytic efficiency.

Herein, we crafted hybrid materials by coating polystyrene (PS) submicrobeads with silver nanospheres. This innovative material manifests a dense concentration of electromagnetic hot spots upon exposure to visible light, establishing a robust platform for plasmonic applications.[11] Following this, a layer of MOF was applied over the plasmonic beads, combining the

T. Zorlu, I. B. Becerril-Castro, R. A. Alvarez-Puebla
Department of Physical and Inorganic Chemistry
Universitat Rovira i Virgili
Tarragona 43007, Spain
E-mail: ramon.alvarez@urv.cat

A. Sousa-Castillo, B. Puértolas, L. V. Besteiro, M. A. Correa-Duarte
CINBIO
Universidade de Vigo
Vigo 36310, Spain
E-mail: macorrea@uvigo.es

Z. Wang
Institute of Fundamental and Frontier Sciences
University of Electronic Science and Technology of China
Chengdu 610054, China

A. Govorov
Department of Physics and Astronomy
Ohio University
Athens, OH 45701, USA

R. A. Alvarez-Puebla
ICREA—Institució Catalana de Recerca i Estudis Avançats
Barcelona 08010, Spain

The ORCID identification number(s) for the author(s) of this article can be found under https://doi.org/10.1002/adfm.202410352

DOI: 10.1002/adfm.202410352

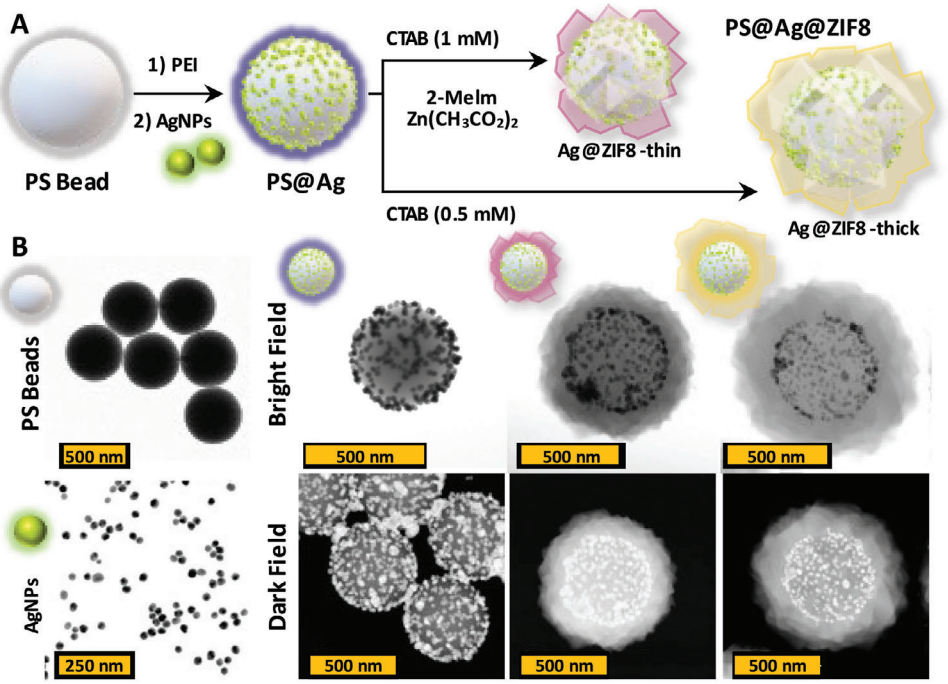

Figure 1. Fabrication and TEM/STEM images of plasmonic-MOFs. A) Schematic procedure followed for the synthesis. B) TEM images of PS beads and AgNPs and STEM images (bright and dark field) for PS@Ag, Ag@ZIF-thin, and thick plasmonic-MOFs.

unique plasmonic properties with the advantageous high porosity and extensive surface area of MOFs. The result of this work is the demonstration of the catalytical properties of metal-organic frameworks through plasmon-induced hot-electrons from the silver nanoparticles, exemplified by the degradation of rhodamine B and the variation of its efficiency as a function of the energy of the light. This assessment was conducted under various lighting conditions, including monochromatic lights at wavelengths of 532, 633, and 785 nm, as well as under the full spectrum of solar light.

2. Results and Discussion

The synthesis of plasmonic MOFs was orchestrated through a layer-by-layer self-assembly process,[12] employing silver nanoparticles (AgNPs) of 26 nm on polystyrene beads of 468 nm to create PS@Ag beads. The use of PS beads not only imparts stability to the system but also facilitates the separation and regeneration of the catalyst after the reaction. Beads were subsequently enveloped in a zeolite imidazolate framework-8 (ZIF-8) layer, resulting in the PS@Ag@ZIF-8 composite (Figure S1, Supporting Information). The entirety of this procedure is illustrated schematically in **Figure 1A**. Initially, the negatively charged PS beads ($\xi = -38$ mV) were modified with polyethyleneimine (PEI), transforming them into positively charged entities ($\xi = +44$ mV). This modification facilitated the electrostatic attraction and subsequent bonding of the negatively charged AgNPs ($\xi = -32$ mV) to the beads. Detailed graphs depicting the ξ-potentials before and after each step are presented in Figure S2 (Supporting Information). The concentration of silver nanoparticles on the polystyrene beads was estimated by counting the number of nanoparticles in several beads images obtained by high-angle annular dark-field scanning transmission electron microscopy (HAADF-STEM) (Figure 1B).

To foster the growth of the ZIF-8 layer around the PS@Ag beads, cetyltrimethylammonium bromide (CTAB) was introduced. Given the known impact of CTAB as a surfactant in altering the morphological characteristics and size of ZIF-8 crystals,[13] its influence during the coating process was thoroughly examined across three distinct concentrations (0.5, 1.0, and 2.0 mM). Observations revealed that the size of the ZIF-8 shells diminished in correlation with the increasing CTAB concentration, with concentrations exceeding the critical micellar concentration of CTAB (1 mM) resulting in incompletely formed shells, as depicted in Figure S3 (Supporting Information). Transmission electron microscopy (TEM) images showcasing the PS beads and AgNPs, alongside scanning transmission electron microscopy (STEM) images of the PS@Ag and PS@Ag@ZIF-8 composites, are highlighted in Figure 1B. To differentiate between the two variants of ZIF-8 shells, henceforth, the plasmonic MOFs will be distinguished as Ag@ZIF-thin and Ag@ZIF-thick, based on the thickness of their ZIF-8 shells, which measured 121 and 179 nm respectively (Figures S3 and S4, Supporting Information).

The composition and elemental distribution within the plasmonic-MOFs were evaluated using energy-dispersive X-ray spectroscopy (EDX). This technique provides detailed insights into the spatial distribution of elements within a sample, crucial for understanding the structural and compositional nuances of the synthesized materials. In **Figure 2**, elemental mapping showcases that the silver nanoparticles are uniformly dispersed across the surface of the beads, with no silver detected within the

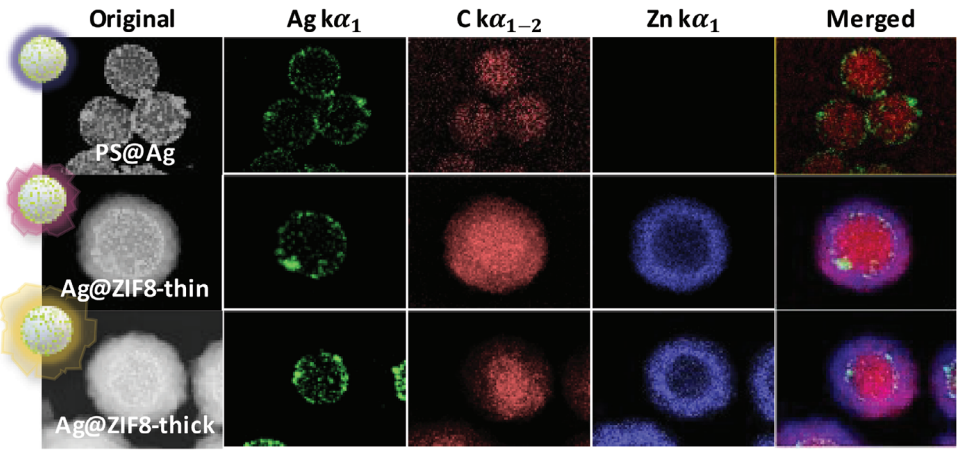

Figure 2. STEM images and EDX composition maps of plasmonic-MOFs. In green, red, and blue the composition distribution of Ag, C, and Zn respectively.

ZIF-8 shell. This finding underscores the efficacy of the encapsulation process using ZIF-8. As anticipated, the presence of Zn is exclusively observed in the samples coated with the ZIF-8 shell, demonstrating the successful incorporation of the ZIF-8 layer.

Powder X-ray diffraction (XRD) patterns were meticulously acquired to further understand the crystalline structure of the synthesized samples (**Figure 3A**). The XRD patterns revealed distinct signals corresponding to the natural sodalite structure of pure crystalline ZIF-8 (depicted in violet), which were prominently observed in both the Ag@ZIF-thin and Ag@ZIF-thick samples. Additionally, the presence of silver within the samples was confirmed by the relatively subdued peaks corresponding to the (111) and (200) planes, indicative of Ag's crystalline structure. In parallel, the nitrogen adsorption isotherms were analyzed (Figure 3B), exhibiting type I isotherms characterized by a sharp uptake at low pressures—a hallmark of microporous structures.[14] Notably, an increase in both the total pore volume and surface area (SBET) was observed, with values approximating 1200 versus 1280 $m^2\ g^{-1}$ for the two types of plasmonic-MOFs, respectively. This variation is reflective of the differing thicknesses of the ZIF-8 shells, yet falls within the expected range for pristine ZIF-8.[15] The congruence in XRD patterns between the two variants of plasmonic-MOFs suggests that they are nearly identical in composition, with the thickness of the ZIF-8 shell being the primary distinguishing factor.

To assess the optical properties of these materials, UV–vis spectroscopy was employed, analyzing aqueous suspensions of the samples (**Figure 4A**). Both, the aggregation of AgNPs on the PS@Ag beads and the higher effective refractive index due to the PS beads, are manifested as a broadening of the absorption band, accompanied by a redshift from the LSPR typical of single AgNPs (from 404 to 441 nm).[16] The incorporation of the ZIF-8 shell induced a further shift in the absorption band, again by increasing the effective refractive index surrounding the AgNPs, and introduced a pronounced absorption peak emerging ≈230 nm arising from its semiconducting properties. Furthermore, the incorporation of AgNPs endowed the composites with SERS activity, as demonstrated in Figure 4B. To evaluate the SERS efficiency, benzenethiol (BT), a conventional molecular probe, was utilized.[17] The limit of detection for all samples was impressively low, at 10^{-12} M, showcasing the efficiency of the generated hot spots and the subsequent the sensitivity. For all samples, the SERS intensities were similar, signaling that the coating with ZIF-8 do not modify the plasmonic surface or the size and porous structure of the MOF.[3b,5d,18]

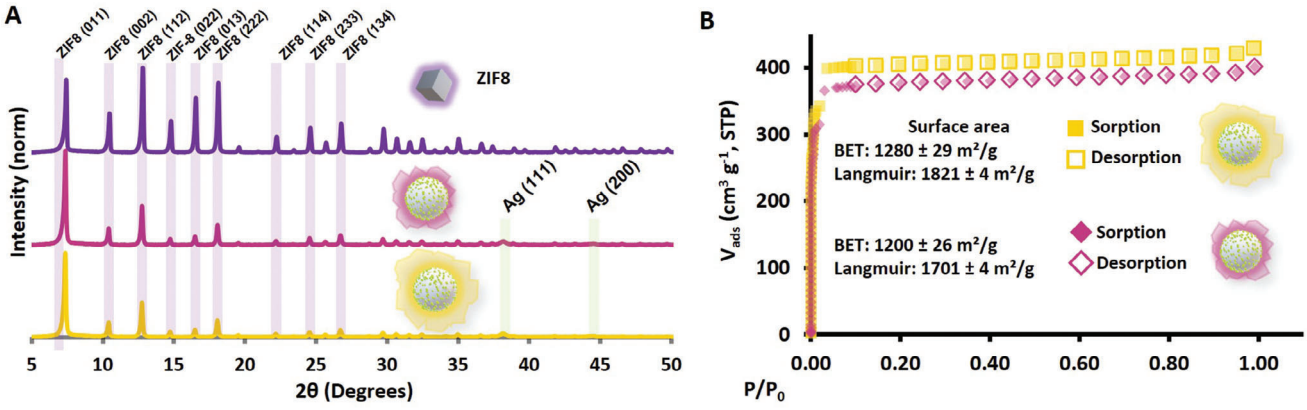

Figure 3. Physical characterization of plasmonic-MOFs. A) X-ray powder diffraction (ZIF-8 included) and B) nitrogen sorption isotherms (77 K).

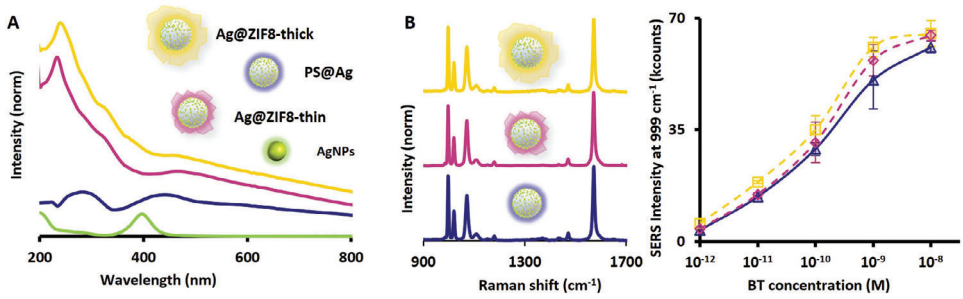

Figure 4. Optical characterization of plasmonic-MOFs. A) UV–vis spectroscopy and B) SERS spectra and detection limits for the PS@Ag, Ag@ZIF-thin, and Ag@ZIF-thick nanocomposites with benzenethiol as molecular probes upon illumination with 532 nm laser light.

Upon comprehensive characterization, the plasmon-induced photocatalytic capabilities of the plasmonic-MOFs were evaluated through the degradation of Rhodamine B (RhB) under the illumination of three different laser wavelengths: 532, 633, and 785 nm using the signal loss in operando SERS. The experimental outcomes, as depicted in **Figure 5**A, reveal a pronounced dependency of the photocatalytic activity on the wavelength of light used, with 532 nm exhibiting the highest activity and 785 nm the lowest. Remarkably, for each wavelength tested, the photocatalytic efficiency at the 60 min mark was greatest for the Ag@ZIF-thick samples, while the PS@Ag samples demonstrated the least efficiency. Furthermore, the photocatalytic behavior of the materials under the irradiation of a solar simulator was investigated, as shown in Figure 5B.

To gain further insight about the process kinetics with the different materials and illumination sources, the kinetic data were modeled with a first-order reaction: Rate = $e^{-\kappa t}$ + constant (Figure 5A,B, doted lines). That is, the reaction rate depends only on the hot-electron concentration but not on the molecular concentration.[19] Indeed, the observed data showed great agreement with the first-order reaction trend. By representing the reaction rate, κ, as a function of the illumination wavelength for the three materials (Figure 5C), three facts become clear. First, the degradation reaction rate increases with the thickness of the MOF, being close to negligible in uncoated materials; second, the degradation strongly depends of the illumination wavelength, and; third, when the monochromatic light's wavelength approaches the single-particle LSPR, exciting the red-shifted modes arising from interparticle coupling, the rate notably increases. In other words, monochromatic light that excites the hybridized localized surface plasmon resonance (LSPR) of interacting AgNPs promotes the generation of hot electrons at the electromagnetic hot spots between the AgNPs. This is clearly observed in our samples, where MOF-coated particles show increased efficiency for light excitation in the following order: 514 nm > 633 nm > solar (white light) > 785 nm. The fact that the MOF coated particles show improved efficiency with respect to uncoated materials points toward the photocatalytical nature of the MOF, which provides catalytic centers to the hybrid.

These results are noteworthy because they highlight the ability of the system to harness photodegradation using photons of significantly lower energy (2.33, 1.96, and 1.58 eV) compared to the band gap of pristine ZIF-8, which is 4.19 eV (3.4 eV for PS@Ag@ZIF-8) as determined by experimental Tauc's plot (Figure S5, Supporting Information). They transparently show that the incorporation of Ag nanoparticles within the ZIF-8 matrix extends the photocatalytic effect onto a broader spectrum by injecting intraband plasmonic hot carriers in the semiconductor, which in turn provides reaction centers. The Ag nanoparticles thus reduce the energy threshold for the photons capable of inducing the reaction, from the value marked by the semiconductor bandgap to the smaller energy barrier between metal and semiconductor (see **Figure 6**A). The observed effect clearly indicates that the reaction rate increases as the interparticle hot spots are excited.[19]

Finally, to test for the stability of the photocatalyst, we conducted a series of four cycles using a solar simulator as the light source Figure S6A (Supporting Information). The exposure of the photocatalyst to multiple cycles of operation demonstrates its good performance and stability under prolonged simulated solar irradiation. These experiments provide valuable insights into the durability and robustness of the photocatalytic system over repeated usage under the experimental conditions described in this work. Analogously, to demonstrate the chemical stability of the compound a thorough analysis of the potential leaching was carried out using inductively coupled plasma optical emission spectroscopy to quantitatively determine the presence of Ag in the supernatants. The results revealed negligible leaching of Ag from the photocatalytic system (Figure S6B, Supporting Information). Furthermore, the supernatant liquids obtained after centrifugation post-reaction demonstrated no catalytic activity, indicating the absence of any significant leached Ag species capable of sustaining catalytic activity.

To assess the formation of hydroxyl radicals (HO•) during the degradation of Rhodamine B (RhB)[20] we used the transformation of terephthalic acid into the fluorescent product 2-hydroxyterephthalic acid as an indicator of hydroxyl radical formation.[21] This methodology allowed us to directly monitor the generation of hydroxyl radicals resulting from the interaction between excited electron-hole pairs and H_2O molecules during the photocatalytic process. The results clearly evidence for the formation of hydroxyl radicals within our PS@ZIF-8 and PS@Ag@ZIF-8 photocatalytic systems (Figure S7, Supporting Information). Upon illumination, hot electrons are generated in the plasmonic metal, which is then injected into the conduction band of ZIF-8, facilitating the formation of the superoxide radical ($O_2^{\bullet -}$) from freely dissolved O_2 in water. These radicals subsequently react with water to produce highly

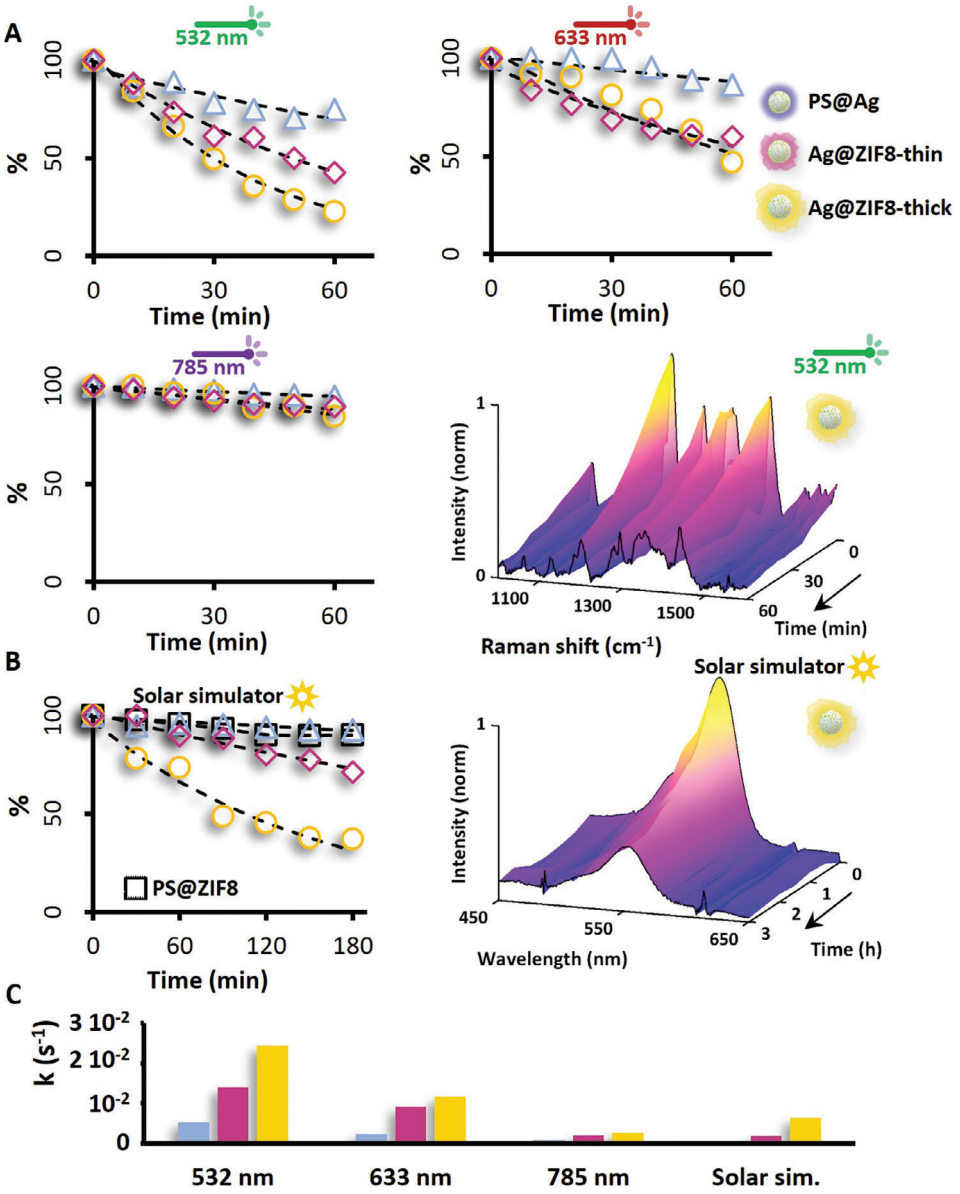

Figure 5. Photocatalytical degradation curves of rhodamine B under different illumination. A) Degradation under monochromatic 532, 633, and 785 nm light. Intensity corresponds to band 1202 cm^{-1}. SERS spectra are presented as a 3D graph to guide the diminishing of the intensity across the full spectrum. B) Degradation under a solar simulator. Fluorescence spectra are presented to guide the diminishing of the intensity. C) Representation of the kinetic rate as a function of the illumination light for all materials. The kinetic rate was extracted from the first order kinetic equation used to fit the SERS and UV/vis kinetic data in the panel above.

reactive hydroxyl radicals (Figure 6A). The almost negligible degradation of RhB in PS@Ag samples outlines that the formation of $^{\bullet}O_2^-$ from the bare plasmonic material is not efficient, suggesting that the injection of electrons from the metal to the ZIF-8 is the most plausible reason, which requires a more in-depth examination.

Initially, mechanisms involving direct optical excitation of ZIF-8, such as those identified in its degradation of methylene blue,[22] might be considered irrelevant, as the energy of the excitation source is below the band gap of ZIF-8, precluding direct light excitation within the ZIF-8 shell. Plasmonic-MOFs have been shown to increase the local concentration of analytes due to ZIF-8's affinity for specific probes,[5d] suggesting that enhanced degradation could result from a higher concentration of reactants near the catalytic sites. However, considering that RhB is a cationic dye featuring polar functional groups such as amino and ether groups, an argument based solely on increased concentration might be insufficient. This is because the ZIF-8 shells carry a positive charge, which would not inherently attract the similarly charged RhB molecules.

To support our understanding of the hybrids' response, the electrodynamic response of the nanostructures was computed using COMSOL Multiphysics, a tool that solves Maxwell's

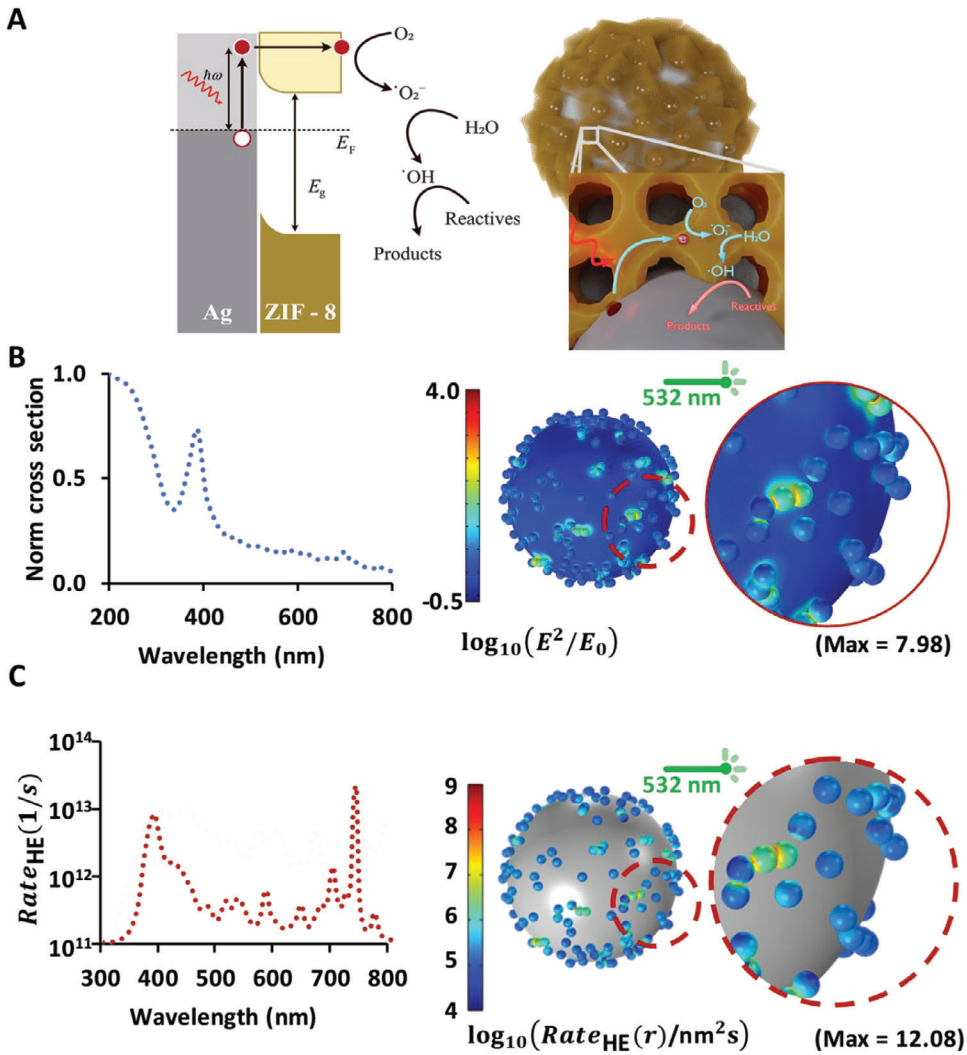

Figure 6. Reaction mechanism and computer simulations with hot carriers. A) Mechanism with hot electrons produced by the AgNPs produces hydroxyl radicals (—OH) that can decompose the RhB. B) Far field extinction spectrum and near field maps under a 532 nm-plane wave excitation, both obtained by averaging over propagation direction and linear polarization. C) Spectrum of total hot electron excitation rates across the hybrid, and map of local rates of excitation when illuminated with 532 nm monochromatic light, again averaged under illumination conditions to mimic average response in solution.

equations through finite element methods (FEM). Figure 6B presents the normalized spectrum of its extinction cross-section, together with field enhancement maps at the surface of the PS and Ag in the Ag@ZIF-8 sample. The extinction shows a pronounced band ≈385 nm arising from the absorption of the AgNPs when exciting single-particle modes. Smaller peaks at longer wavelengths are due to multi-particle modes caused by NP aggregates on the bead's surface. The near-field map highlights regions of enhanced field strength where AgNPs are in close proximity and create interparticle hot spots.[16] Figure 6C plots the rate of hot carrier production, with large energies sufficient to abandon the metal and generate $O_2^{\bullet-}$ species, demonstrating that the presence of AgNPs extends carrier production across the visible spectrum. Despite Figure 6C showing peaks above the 500 nm wavelength, which are caused by specific NP aggregates in this model with randomly distributed AgNPs, a general trend toward reduced hot electron generation at lower energy levels is evident. One can understand this trend by considering that longer-wavelength modes require a longer quasi-linear concatenation of AgNPs, therefore being more unlikely than single-particle modes and dimers.

These results therefore suggest that the diminished degradation of RhB under longer wavelength illumination, as seen in Figure 5, is a direct consequence of decreased hot electron production with longer wavelengths within the plasmonic-MOFs. The overall agreement between the main features of experimental and computational results provides insights into the underlying mechanisms driving photocatalytic degradation by these advanced materials, which in turn underscore the potential of plasmonic-MOFs in environmental remediation and sustainable chemistry applications, where efficient light-driven processes are essential.

3. Conclusion

Plasmonic metal-organic frameworks herald a significant advancement in the realm of photocatalysis by integrating the generation of hot carriers through localized surface plasmon resonance excitation across the visible spectrum. The photostability of PS@Ag nanoparticles in isolation exhibited minimal degradation; however, upon incorporation of ZIF-8, a substantial enhancement in photodegradation was observed. This pivotal finding underscores the synergistic effect resulting from the simultaneous action of high-energy injection and the multifunctionality of the MOF. Further, the photocatalytic activity increases as the excitation line approaches the localized surface plasmon resonance. The potential applications of plasmonic-MOFs extend far beyond environmental remediation to include areas such as energy conversion, sensing, and the synthesis of value-added chemicals, each benefiting from the enhanced photocatalytic capabilities of these materials. As research in this field continues to evolve, plasmonic-MOFs are poised to play a pivotal role in the transition toward more sustainable and efficient catalytic processes.

Supporting Information

Supporting Information is available from the Wiley Online Library or from the author.

Acknowledgements

This work was supported by the projects PID2020-118282RA-I00-I00/AEI/10.13039/501100011033, PID2020-120306RB-I00/AEI/10.13039/501100011033, PID2020-113704RB-I00/AEI/10.13039/501100011033; TED2021-130038A-I00, TED2021-132101B-I00, RYC2021-033818-I, RYC2021-032910-I, PDC2021-121787-I00 funded by MCIN/AEI/10.13039/501100011033 and European Union "NextGenerationEU"/PRTR; Xunta de Galicia (Centro Singular de Investigación de Galicia – Accreditation 2019–2022 and ED431C 2022/24); 2020SGR00166 (funded by Generalitat de Cataluña), 2021PFR-URV-B2-02 (funded by Universitat Rovira i Virgili), and HORIZON-EIC-2022-PATHFINDERCHALLENGES-01-06, HORIZON-HLTH-2022-DISEASE-06-TWO-STAGE, GA. No. 857543 and ENSEMBLE3 – Centre of Excellence for nanophotonics, advanced materials and novel crystal growth-based technologies" project (GA No. MAB/2020/14) of the European Union Horizon 2020 Research and Innovation Program.

Conflict of Interest

The authors declare no conflict of interest.

Data Availability Statement

The data that support the findings of this study are available from the corresponding author upon reasonable request.

Keywords

AgNPs, hot-carrier injection, hot-electrons, MOFs, photocatalysis, ZIF-8

Received: June 13, 2024
Revised: July 8, 2024
Published online: July 25, 2024

[1] a) H. Furukawa, N. Ko, Y. B. Go, N. Aratani, S. B. Choi, E. Choi, A. O. Yazaydin, R. Q. Snurr, M. O'Keeffe, J. Kim, O. M. Yaghi, *Science* **2010**, *329*, 424; b) N. Stock, S. Biswas, *Chem. Rev.* **2012**, *112*, 933.

[2] a) L. He, Y. Liu, J. Liu, Y. Xiong, J. Zheng, Y. Liu, Z. Tang, *Angew. Chem., Int. Ed.* **2013**, *52*, 3741; b) G. Zheng, S. de Marchi, V. López-Puente, K. Sentosun, L. Polavarapu, I. Pérez-Juste, E. H. Hill, S. Bals, L. M. Liz-Marzán, I. Pastoriza-Santos, J. Pérez-Juste, *Small* **2016**, *12*, 3935; c) C. Koh, O. Sim, S. X. Leong, S. K. Boong, C. R. C. Chong, X. Y. Ling, *ACS Mater. Lett.* **2021**, *3*, 557.

[3] a) P. Horcajada, T. Chalati, C. Serre, B. Gillet, C. Sebrie, T. Baati, J. F. Eubank, D. Heurtaux, P. Clayette, C. Kreuz, J. S. Chang, Y. K. Hwang, V. Marsaud, P. N. Bories, L. Cynober, S. Gil, G. Férey, P. Couvreur, R. Gref, *Nat. Mater.* **2010**, *9*, 172; b) C. Carrillo-Carrión, R. Martínez, M. F. Navarro Poupard, B. Pelaz, E. Polo, A. Arenas-Vivo, A. Olgiati, P. Taboada, M. G. Soliman, Ú. Catalán, S. Fernández-Castillejo, R. Solà, W. J. Parak, P. Horcajada, R. A. Alvarez-Puebla, P. del Pino, *Angew. Chem., Int. Ed.* **2019**, *58*, 7078.

[4] a) D. Peralta, G. Chaplais, A. Simon-Masseron, K. Barthelet, C. Chizallet, A.-A. Quoineaud, G. D. Pirngruber, *J. Am. Chem. Soc.* **2012**, *134*, 8115; b) D. Peralta, G. Chaplais, J.-L. Paillaud, A. Simon-Masseron, K. Barthelet, G. D. Pirngruber, *Micropor. Mesopor. Mater.* **2013**, *173*, 1; c) Q. Qian, P. A. Asinger, M. J. Lee, G. Han, K. Mizrahi Rodriguez, S. Lin, F. M. Benedetti, A. X. Wu, W. S. Chi, Z. P. Smith, *Chem. Rev.* **2020**, *120*, 8161; d) L. B. T. Nguyen, Y. X. Leong, C. S. L. Koh, S. X. Leong, S. K. Boong, H. Y. F. Sim, G. C. Phan-Quang, I. Y. Phang, X. Y. Ling, *Angew. Chem., Int. Ed.* **2022**, *61*, 202207447.

[5] a) C. S. L. Koh, H. K. Lee, X. Han, H. Y. F. Sim, X. Y. Ling, *Chem. Comm.* **2018**, *54*, 2546; b) H. K. Lee, C. S. Koh, W.-S. Lo, Y. Liu, I. Y. Phang, H. Y. Sim, Y. H. Lee, G. C. Phan-Quang, X. Han, C.-K. Tsung, X. Y. Ling, *J. Am. Chem. Soc.* **2020**, *142*, 11521; c) T. Zorlu, B. Puértolas, I. B. Becerril-Castro, L. Guerrini, V. Giannini, M. A. Correa-Duarte, R. A. Alvarez-Puebla, *ACS Nanoscience Au* **2023**, *3*, 222; d) T. Zorlu, I. B. Becerril-Castro, B. Puertolas, V. Giannini, M. A. Correa-Duarte, R. A. Alvarez-Puebla, *Angew Chem Int Ed* **2023**, *62*, 202305299.

[6] J. Langer, D. Jimenez de Aberasturi, J. Aizpurua, R. A. Alvarez-Puebla, B. Auguié, J. J. Baumberg, G. C. Bazan, S. E. J. Bell, A. Boisen, A. G. Brolo, J. Choo, D. Cialla-May, V. Deckert, L. Fabris, K. Faulds, F. J. García de Abajo, R. Goodacre, D. Graham, A. J. Haes, C. L. Haynes, C. Huck, T. Itoh, M. Käll, J. Kneipp, N. A. Kotov, H. Kuang, E. C. Le Ru, H. K. Lee, J.-F. Li, X. Y. Ling, et al., *ACS Nano* **2020**, *14*, 28.

[7] a) M. L. Brongersma, N. J. Halas, P. Nordlander, *Nat. Nanotechnol.* **2015**, *10*, 25; b) H. Jin, M. Herran, E. Cortés, J. Lischner, *ACS Photonics* **2023**, *10*, 3629.

[8] a) Y. Negrín-Montecelo, A. H. A. Geneidy, A. O. Govorov, R. A. Alvarez-Puebla, L. V. Besteiro, M. A. Correa-Duarte, *ACS Photonics* **2023**, *10*, 3310; b) Y. Negrín-Montecelo, X.-T. Kong, L. V. Besteiro, E. Carbó-Argibay, Z. M. Wang, M. Pérez-Lorenzo, A. O. Govorov, M. Comesaña-Hermo, M. A. Correa-Duarte, *ACS Appl. Mater. Interfaces* **2022**, *14*, 35734; c) A. Movsesyan, E. Y. Santiago, S. Burger, M. A. Correa-Duarte, L. V. Besteiro, Z. Wang, A. O. Govorov, *Adv. Opt. Mater.* **2022**, *10*, 2102663.

[9] a) M. Alvaro, E. Carbonell, B. Ferrer, F. X. Llabrés I Xamena, H. Garcia, *Chemistry – A European Journal* **2007**, *13*, 5106; b) Z. Li, J. Zi, X. Luan, Y. Zhong, M. Qu, Y. Wang, Z. Lian, *Adv. Funct. Mater.* **2023**, *33*, 2303069; c) X.-M. Cheng, P. Wang, S.-Q. Wang, J. Zhao, W.-Y. Sun, *ACS Appl. Mater. Interfaces* **2022**, *14*, 32350.

[10] X. Zeng, L. Huang, C. Wang, J. Wang, J. Li, X. Luo, *ACS Appl. Mater. Interfaces* **2016**, *8*, 20274.

[11] a) D. Tsoutsi, J. M. Montenegro, F. Dommershausen, U. Koert, L. M. Liz-Marzán, W. J. Parak, R. A. Alvarez-Puebla, *ACS Nano* **2011**, *5*, 7539; b) I. B. Becerril-Castro, V. Salgueiriño, M. A. Correa-Duarte, R. A. Alvarez-Puebla, *Adv. Funct. Mater.* **2024**, *34*, 2314084.

[12] E. Pazos, M. Garcia-Algar, C. Penas, M. Nazarenus, A. Torruella, N. Pazos-Perez, L. Guerrini, M. E. Vázquez, E. Garcia-Rico, J. L.

Mascareñas, R. A. Alvarez-Puebla, *J. Am. Chem. Soc.* **2016**, *138*, 14206.
[13] Y. Pan, D. Heryadi, F. Zhou, L. Zhao, G. Lestari, H. Su, Z. Lai, *CrystEngComm* **2011**, *13*, 6937.
[14] a) M. He, J. Yao, Q. Liu, K. Wang, F. Chen, H. Wang, *Microporous Mesoporous Mater.* **2014**, *184*, 55; b) K. Zhou, B. Mousavi, Z. Luo, S. Phatanasri, S. Chaemchuen, F. Verpoort, *J. Mater. Chem. A* **2017**, *5*, 952.
[15] D. Zou, D. Liu, J. Zhang, *Energy Environ. Mater.* **2018**, *1*, 209.
[16] M. Rycenga, P. H. C. Camargo, W. Li, C. H. Moran, Y. Xia, *J. Phys. Chem. Lett.* **2010**, *1*, 696.
[17] M. Blanco-Formoso, A. Sousa-Castillo, X. Xiao, A. Mariño-Lopez, M. Turino, N. Pazos-Perez, V. Giannini, M. A. Correa-Duarte, R. A. Alvarez-Puebla, *Nanoscale* **2019**, *11*, 21872.
[18] R. A. Álvarez-Puebla, R. Contreras-Cáceres, I. Pastoriza-Santos, J. Pérez-Juste, L. M. Liz-Marzán, *Angew. Chem., Int. Ed.* **2009**, *48*, 138.
[19] L. Nan, J. Giráldez-Martínez, A. Stefancu, L. Zhu, M. Liu, A. O. Govorov, L. V. Besteiro, E. Cortés, *Nano Lett.* **2023**, *23*, 2883.
[20] J. Zhuang, W. Dai, Q. Tian, Z. Li, L. Xie, J. Wang, P. Liu, X. Shi, D. Wang, *Langmuir* **2010**, *26*, 9686.
[21] A. Sousa-Castillo, J. R. Couceiro, M. Tomás-Gamasa, A. Mariño-López, F. López, W. Baaziz, O. Ersen, M. Comesaña-Hermo, J. L. Mascareñas, M. A. Correa-Duarte, *Nano Lett.* **2020**, *20*, 7068.
[22] D. Saliba, M. Ammar, M. Rammal, M. Al-Ghoul, M. Hmadeh, *J. Am. Chem. Soc.* **2018**, *140*, 1812.